PCCP

ROYAL SOCIETY OF CHEMISTRY

PAPER

View Article Online
View Journal | View Issue

Cite this: *Phys. Chem. Chem. Phys.*, 2022, **24**, 21722

Anisotropic thermal transport in twisted bilayer graphene†

Wenxiang Liu,[a] Yang Hong,[b] Jingchao Zhang *[c] and Yanan Yue*[a]

Received 25th April 2022,
Accepted 24th August 2022

DOI: 10.1039/d2cp01896a

rsc.li/pccp

Recently, twisted bilayer graphene (TBLG) has attracted enormous attention owing to its peculiar electronic properties. In this work, the anisotropic thermal conductivity of TBLG is comprehensively investigated. It is reported that interlayer twisting can be a practical approach for thermal transport regulation with high accuracy. A strong non-monotonic correlation between anisotropic thermal conductivity and twisting angles is revealed. Extensive phonon behavior analyses reveal the physical mechanism. The anisotropic thermal transport in TBLG is explained by the calculated phonon density of states (PDOS). Meanwhile, the phonon spectra and phonon relaxation times extracted from spectral energy density (SED) profiles explain the decreasing trend of thermal conductivity with increasing twisting angles. The increase in thermal conductivity is attributed to the combined effects of twist and anisotropy. The reported anisotropic thermal conductivity is important to the thermal modulation and our analyses provide a valuable complement to the phonon studies of TBLG.

1. Introduction

Since the discovery of graphene,[1] it has gained widespread attention due to its unique electrical,[2] mechanical[3] and thermal properties.[4] As a promising material, graphene possesses an ultrahigh electron mobility[5] of approximately 20 000 $cm^2\ V^{-1}\ s^{-1}$ and a thermal conductivity[6] of 4000 $W\ m^{-1}\ K^{-1}$. The number of layers affecting the properties of graphene has also been extensively studied.[7–10] Through measurements and calculations, it was found that bilayer graphene possesses a tunable band gap,[11] which overcomes the drawback of lacking a band gap in single-layer graphene.

Interlayer twisting has been proven to be an effective approach for manipulating the electrical,[12] optical[13] and thermal properties.[14,15] In particular, the observation of superconductivity[16] in twisted bilayer graphene (TBLG) when the twisting angle is near 1.1° has spurred the research interest in this peculiar Moiré pattern structure.[17,18] In addition, the band gap of TBLG is tunable by inserting alkali metal atoms and controlling the rotation angle.[19] For optical properties, Anh Le *et al.*[20] calculated the electronic structure and optical properties of TBLG and found that the optical conductivity of TBLG has a strong relationship with the twisting angle. And in the small angle region, as the angle gradually tends to 0°, the W-shape density of states transforms into a U-shape. Raman spectroscopy of TBLG which plays a crucial role in materials optical and phonon analysis has been explored by Campos-Delgado *et al.*[21] The phonon dispersion of TBLG was probed by Raman scattering induced by twisting angle dependent wavevector. And the ZO′ phonons activated by the Moiré pattern were discovered.

Anisotropic thermal conductivity has been widely observed in numerous materials, such as graphene,[22] diamond films,[23] single crystal β-gallium oxide,[24] *etc.* For this peculiar physical property, numerous experiments and theoretical calculations were employed to explore the involved physical mechanism. Renteria *et al.*[25] measured the thermal conductivity of reduced graphene oxide annealed at high temperatures. After high-temperature annealing, the dramatic increase in the in-plane thermal conductivity contrasts with the decrease in the out-of-plane thermal conductivity, which shows the unexpectedly strong anisotropy of the reduction of graphene oxide. The increase in the in-plane thermal conductivity and the decrease of out-of-plane thermal conductivity were attributed to the reduced phonon scattering to oxygen atoms and other impurities and the appearance of air pockets. Ye *et al.*[26] performed molecular dynamics (MD) simulation to calculate the thermal conductivity of body-centered tetragonal C_4. The cross-plane and in-plane thermal conductivity can reach about 1209 $W\ m^{-1}\ K^{-1}$ and 738 $W\ m^{-1}\ K^{-1}$ which show the high anisotropic thermal conductivity. Jang *et al.*[27] measured the thermal conductivity of passivated black phosphorus by using the time-domain thermo-reflectance method. The anisotropic thermal conductivity was found as follows: the in-plane thermal

[a] *Key Laboratory of Hydraulic Machinery Transients (MOE), School of Power and Mechanical Engineering, Wuhan University, Wuhan, Hubei 430072, China. E-mail: yyue@whu.edu.cn*
[b] *Research Computing, RCAC, Purdue University, West Lafayette, IN 47907, USA*
[c] *Microsoft Corporation, Redmond, WA 98052, USA. E-mail: jingczhang@microsoft.com*

† Electronic supplementary information (ESI) available. See DOI: https://doi.org/10.1039/d2cp01896a

conductivity was 86 W m^{-1} K^{-1} for the zigzag direction and 34 W m^{-1} K^{-1} for the armchair direction, which are much higher than 4.0 W m^{-1} K^{-1} for the out-of-plane direction. Although all these materials have been reported to possess high thermal conductivity and various anisotropies, the pursuit of accurate control of anisotropic thermal conductivity of materials is important for phonon engineering and thermal modulation.

This work is aimed at developing a high-fidelity and high-accuracy anisotropic thermal transport regulation method in bilayer graphene by interlayer-twisting. MD simulation revealed a strong correlation of the twisting angle and anisotropic thermal conductivity. The mechanisms underneath this correlation were thoroughly analyzed by examining the phonon behaviors. By calculating the phonon density of states and spectral energy density, we have found that the PDOS values are diverse along different heat flux directions which confirm the anisotropy of TBLG. Furthermore, by using the Lorentz fitting, the phonon relaxation time is calculated to support the finding. Finally, the size effect is considered and the mean free path is acquired by fitting the relationship between thermal conductivity and length variation.

2. Methodology

The system configuration of TBLG is similar to the modeling approach from a previous work.[14] Suspended monolayer graphene is set as the bottom layer and another identical monolayer is stacked on top. The later stacked monolayer graphene will be rotated around the geometric center to the desired angle to create different twisting angles. The structures of AA-stacked bilayer graphene and 10°, 20° and 30° TBLG are illustrated in Fig. 1. The Moiré pattern can be clearly seen after rotation. In addition, it is worth noting from Fig. 1 that lattice parameters are changed due to the rotation.[28] For example, if the twisting angle is equal to 21.78°, the lattice parameters[29] increase from

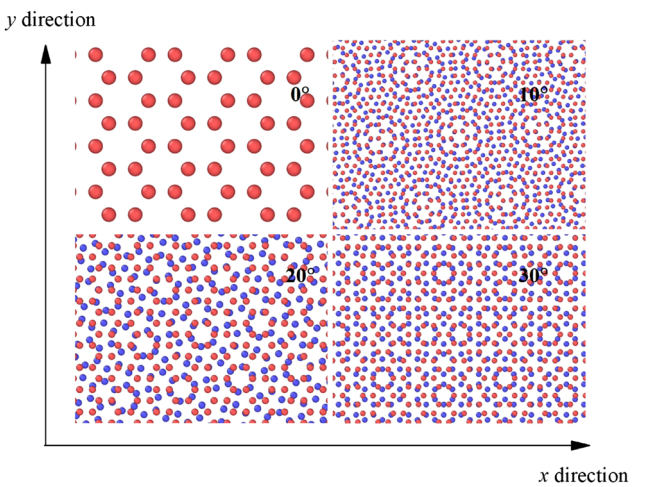

Fig. 1 Moiré pattern of twisted bilayer graphene with different twisting angles. Red and blue colors represent the atom of the top layer and bottom layer, respectively.

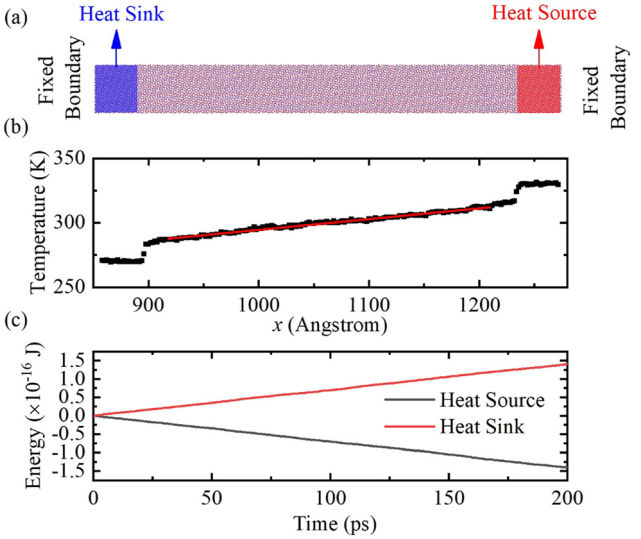

Fig. 2 (a) Schematic diagram of the NEMD method. (b) Temperature distribution (black dot) and temperature fitting (red line) at thermal equilibrium state. (c) Variation of heat source and heat sink energy with time.

2.46 to 6.51 Å. To investigate the anisotropy, the TBLG nanoribbons are cut off at the same length and width along the x and y directions, respectively, based on a large area of TBLG, as shown in Fig. 2(a). The length and width are chosen to be 20 nm and 10 nm, respectively, and the thickness is set twice that of the monolayer thickness size.

All the simulations are performed in a Large-scale Atomic/Molecular Massively Parallel Simulator[30] (LAMMPS). The optimized Tersoff potential[31] is used to model the intralayer C–C interactions which is expressed as:

$$E = \frac{1}{2}\sum_{i}\sum_{i\neq j} V_{ij} \tag{1}$$

$$V_{ij} = f_C(r_{ij})[f_R(r_{ij}) + b_{ij} f_A(r_{ij})] \tag{2}$$

where E is the total energy and V_{ij} represents the potential energy. f_R and f_A are competing attractive and repulsive pairwise terms while f_A includes three-body terms and f_C is a cut-off term. For interlayer van der Waals (vdW) interaction, it is always modeled by the Lennard-Jones potentials[32] expressed as:

$$V(r) = 4\chi\varepsilon\left[\left(\frac{\sigma}{r}\right)^6 - \left(\frac{\sigma}{r}\right)^{12}\right] \tag{3}$$

where χ is the coupling factor, ε is the energy in the equilibrium position and σ is the distance where the force equals zero. The ε and σ parameters in this study are consistent with past research[33] where ε_{C-C} = 4.56 meV and σ_{C-C} = 3.431 Å.

The non-equilibrium molecular dynamics (NEMD) method is employed to calculate the thermal conductivity of TBLG. The detailed setting of simulation and the specific implementation process of the NEMD method are described below. As shown in Fig. 2(a), the fixed boundary condition is applied in the length direction. Meanwhile, the free boundary condition is used in

width and out-of-plane directions, allowing the interlayer distance to change. The time step and cutoff distance are set as 0.5 fs and 12.5 Å, respectively. Establishing a steady state temperature gradient is the central idea of the NEMD method. First, under a canonical ensemble (*NVT*), the Nose–Hoover thermostat is employed to relax the whole system to the target temperature of 300 K. After 500 ps relaxation, the microcanonical ensemble (*NVE*) is used to maintain the total energy of the entire system and check whether the temperature is in equilibrium. Once reaching the thermal equilibrium, the hot and cold Langevin thermostats are added to the two ends of the TBLG nanoribbon as shown in Fig. 2(a). The length of the heat sink and the heat source is 1.5 nm. The Langevin thermostat is applied for 1.5 ns before data collection to ensure a stable temperature gradient. The temperature gradient along the heat flux direction and the variation of heat flux with time are obtained by outputting 200 ps of temperature and energy change. The results are plotted in Fig. 2(b) and (c), and a stable temperature gradient and the same heat flux can be found, which indicates that a new equilibrium has been reached. Therefore, the thermal conductivity can be calculated by Fourier's law which is expressed as:

$$\frac{dQ}{dt} = \kappa A \frac{dT}{dx} \quad (4)$$

where dQ/dt means the heat flux and dT/dx denotes the temperature gradient. A represents the cross-sectional area of TBLG. The calculation of T distribution is acquired from the local kinetic energy average.

3. Results and discussion

3.1 Effect of interlayer twisting on thermal conductivity

The thermal conductivity along different directions, including x and y, is calculated to investigate the anisotropic TBLG. The variation of twisting angle and anisotropic thermal conductivity is demonstrated in Fig. 3. For bilayer graphene with the twisted angle being equal to 0, the thermal conductivity along the y-direction (zigzag) is slightly higher than that in the x-direction (armchair) which is consistent with the previous article.[34] In both x and y directions, the thermal conductivity tends to decrease and then increases with increasing twisting angles. For example, if the heat flux direction is along the x direction, the thermal conductivity decreases from ~361 W m^{-1} K^{-1} to ~289 W m^{-1} K^{-1} and then increases to ~473 W m^{-1} K^{-1}. For the y direction, the values are 627 W m^{-1} K^{-1}, 355 W m^{-1} K^{-1} and 470 W m^{-1} K^{-1}. It is worth mentioning that the calculated thermal conductivity of TBLG is greatly less than that of monolayer graphene. The reasons are mostly included in two aspects, the disruption of the initial lattice structure and layer dependence. The former reason will be discussed in the following section. For layer dependence, numerous research has indicated that with the increase in the number of layers, the thermal conductivity will decrease. Zhong *et al.*[35] have reported that as the layer number increases from one to two, the thermal conductivity will decrease from ~2250 W m^{-1} K^{-1} to 700 W m^{-1} K^{-1}.

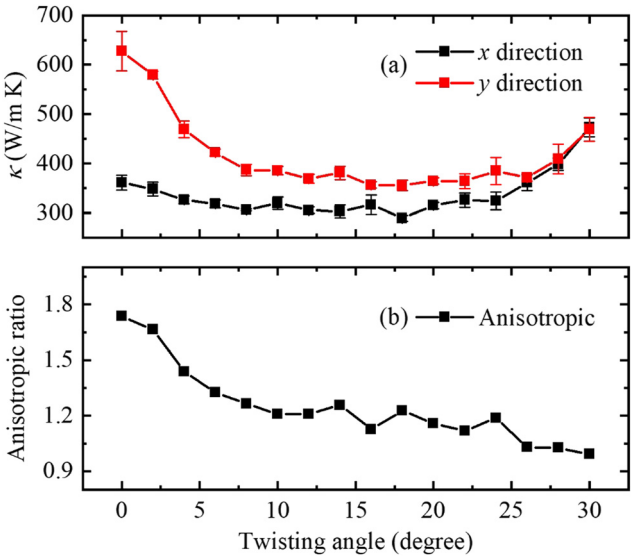

Fig. 3 (a) Thermal conductivity of twisted bilayer graphene with different twisting angles from 0° to 30° along the x direction (black line) and y direction (red line). (b) Anisotropic ratio (κ_y/κ_x) varies with twisting angles.

In addition, the ratios (κ_y/κ_x) of the change in thermal conductivity with twisting angles for different directions are calculated to measure the anisotropy of the TBLG, which is indicated in Fig. 3(b). The anisotropy and twisting angle of TBLG show a strong correlation in numerical correspondence, displaying a one-to-one correspondence. The anisotropy ratio gradually decreases as the twisting angle increases, and finally at 30°, the thermal conductivity values along the x-direction and y-direction are approximately equal, which gives the possibility of precise regulation of the anisotropy of the material. Meanwhile, the larger anisotropic ratio in bilayer graphene compared to that of monolayer graphene can be ascribed to three reasons. The first one is the plunged thermal conductivity due to the increasing number of layers. Under the same conditions, monolayer graphene's thermal conductivity is higher than bilayer graphene's. In bilayer graphene, the interlayer coupling breaks the reflection symmetry and reduces the contribution of out-of-plane acoustic (ZA) phonons to thermal conductivity.[36] In addition, the marginalized phonons and boundary diffusion impair the thermal transport of the phonons, resulting in higher thermal conductivity along the y-direction than in the x-direction.[37] The final reason comes from how the anisotropic ratio is calculated, *i.e.*, the gap between κ_y and κ_x and the value of κ_x. There will be a scenario where the gap reduction is lower than that of κ_x causing the ratio to increase.

3.2 Phonon analysis

Phonon actions are analyzed to reveal the thermal transport mechanism in TBLG by calculating the PDOS and spectral energy density[38] (SED). The PDOS reflects the change in the

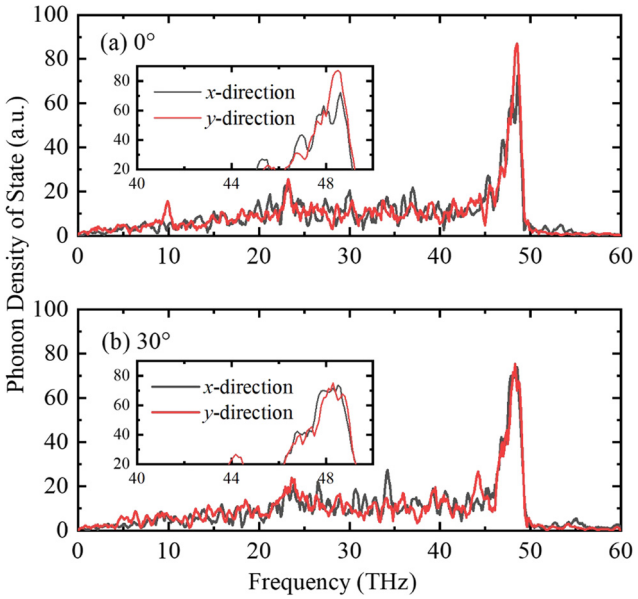

Fig. 4 PDOS of (a) bilayer graphene and (b) twisted bilayer graphene in *x*-direction (black line) and *y*-direction (red line). Small box diagrams illustrate the PDOS near the peak position.

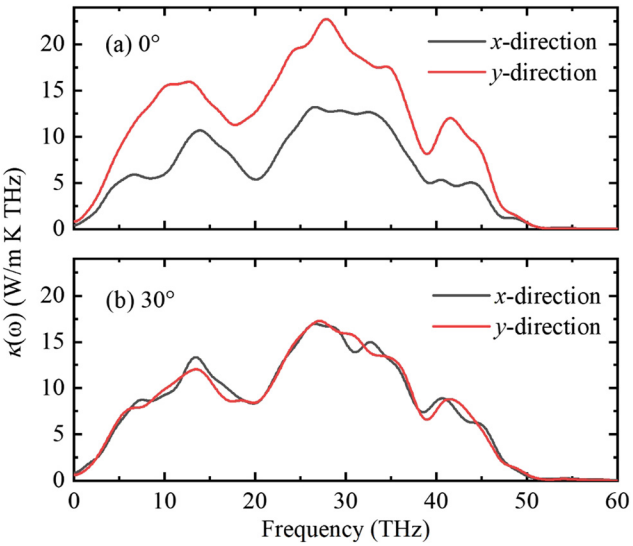

Fig. 5 Frequency dependent thermal conductivity of twisted bilayer graphene with different twisting angles (a) 0° and (b) 30°.

internal vibration pattern of the system which can be calculated by performing the fast Fourier transform (FFT) of the velocity–velocity auto correlation function (VACF) which can be obtained from the MD trajectory of atoms.

$$F(\omega) = \frac{1}{\sqrt{2\pi}}\int_{-\infty}^{+\infty}\frac{\langle v(0)\cdot v(t)\rangle}{\langle v(0)\cdot v(0)\rangle}e^{i\omega t}dt \quad (5)$$

where $\langle v(0)\cdot v(t)\rangle$ is the VACF and F represents the phonon number with frequency between $(\omega, \Delta\omega)$. Fig. 4 indicates the calculated PDOS of (a) bilayer graphene and (b) TBLG with a twisting angle of 30°, and the different directions are distinguished by the red and black lines, respectively. It can be seen that the PDOS lines are all similar in shape which have approximately the same peak positions and maximum frequency values, while the main difference appears at the peak region. For bilayer graphene, the PDOS values in the *y* direction are much higher than in the *x* direction. Larger PDOS values mean that more phonons are involved in thermal transport, which leads to higher thermal conductivity and explains the higher thermal conductivity along the *y*-direction. For 30° TBLG, the PDOS values are equivalent which is consistent with the trends in the calculation of thermal conductivity. In addition, frequency-dependent thermal conductivity is calculated to provide a vivid comparison and the results are illustrated in Fig. 5. The details of the calculation process of frequency-dependent thermal conductivity are given in the ESI.† As shown in Fig. 5, for the twisting angle of 0°, the spectral decomposition thermal conductivity along the *y* direction is essentially greater than that along the *x* direction, although the phonon contributions at different frequencies are different. However, for the twisting angle of 30°, the spectral decomposition thermal conductivity in different directions is approximately the same.

The SED of bilayer graphene and TBLG is subsequently calculated to provide more detailed phonon information, which can predict the phonon dispersion and related phonon relaxation times. The SED calculation requires lattice parameters but not all twisting angles have the corresponding crystalline cell, which must conform to the following equation.[39,40]

$$\cos\theta(m,n) = \frac{(3m^2 + 3mn + n^2/2)}{(3m^2 + 3mn + n^2)} \quad (6)$$

where m and n are positive integers. We selected the TBLG with both m and n equal to 1, corresponding to the twisting angle of 21.78° to calculate its SED. Meanwhile, structures of other twisting angles are shown in the ESI.† The same unrotated bottom layers are chosen to quantify the effect of comparison rotation. Spectral energy density[38] can be calculated based on the equation:

$$\Phi(k,\omega) = \frac{1}{4\pi\tau_0 N_T}\sum_{\alpha}\sum_{b}^{B} m_b\left|\int_0^{\tau_0}\sum_{n_{x,y,z}}^{N_T} v_\alpha\begin{pmatrix} n_{x,y,z} \\ b \end{pmatrix}; t\right) \times \exp\left[ikr\begin{pmatrix} n_{x,y,z} \\ 0 \end{pmatrix} - i\omega t\right]\Bigg|^2 dt \quad (7)$$

where k and ω are the wave vector and frequency, respectively. τ_0 is the total time and N_T is the total number of unit cells. v represents the velocity of atoms and m is the mass. r is the equilibrium position of each unit cell. The specific calculation setup parameters are as follows: the total number of unit cells is 28 and the resolution of frequency and wave vector are set as 0.005 THz and 1/14 (π/a), respectively, where a is the lattice constant that is equal to 2.46 Å here. And the frequency ranges 0–60 THz are calculated, which is enough to show all phonon branches. The velocities of atoms are acquired from the

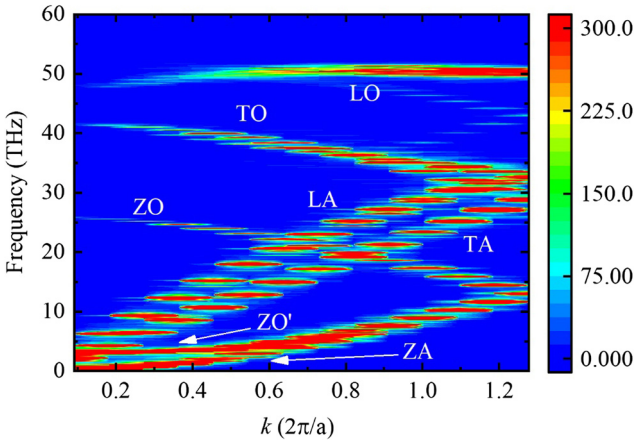

Fig. 6 SED of twisted bilayer graphene with 0°. Six branches familiar with graphene are found, including ZA, TA, LA, ZO, TO and LO. The existence of the ZO′ branch is due to the weak Vdw interaction.

microcanonical ensemble at the temperature of 300 K. The final results are plotted in Fig. 6. For 0° TBLG, the calculated SED is consistent with the phonon dispersion of bilayer graphene calculated with opt-Tersoff potentials,[41] which include six lines denoting different branches, respectively. Small splitting due to weak interlayer interactions was also found near the Γ point, splitting from the ZA branch into the ZA and ZO′ branches.[42,43] The SED of TBLG with a twisting angle of 21.78° is similar to that of 0° TBLG. And the details of branch shift are discussed below.

Moreover, as shown in Fig. 7, the shape of this frequency distribution for each mode is the Lorentz function and the phonon relaxation time can be acquired by using the Lorentz fitting. The Lorentz function is expressed as:

$$\Phi(k,\omega) = \frac{I}{1+[(\omega-\omega_c)/\gamma]^2} \quad (8)$$

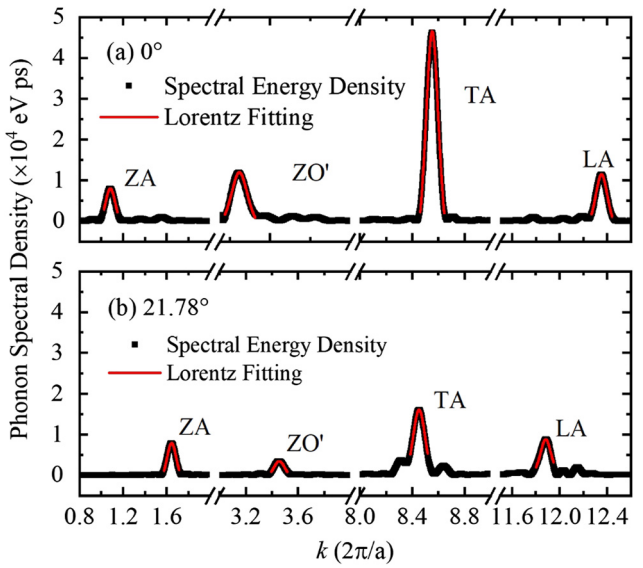

Fig. 7 Detailed SED near the Γ-point of twisted bilayer graphene of (a) 0° and (b) 21.78°and four branches, including the ZA, TA, LA and ZO′, are fitted by Lorentz function, which are denoted in red color lines.

where I is the peak magnitude, ω_c is the peak frequency and γ represents the half-width at half-maximum. And then, the phonon relaxation time is defined as: $\tau = 1/2\gamma$. Fig. 7 shows an example of detailed SED near the Γ point, where Fig. 7(a) shows the result of 0° TBLG and Fig. 7(b) shows the SED of 21.78° TBLG. In both Fig. 7(a) and (b), four peaks which denote different phonon branches, including ZA, TA, LA and ZO′ branches, can be clearly found. However, due to the influence of rotation, the location of the peak position is shifted. The intensity of the spikes decreases while the width increases. Meanwhile, the fitting profiles are denoted in red color which demonstrate the good fitting in SED. The total fitting phonon relaxation times under 15 THz are shown in Fig. 8. Different color dots represent the phonon relaxation times of different branches and the hollow points denote the calculation results of 21.78° TBLG. It can be clearly observed that the phonon relaxation time at 0° is greater than that at 21.78°. The calculated average phonon relaxation time of 0° TBLG is 8.23 ps and for TBLG with twisting angles of 21.78°, the value is 6.90 ps. The max relaxation time of 0° TBLG can reach about 12 ps but for 21.78° TBLG, the phonon time floats around 6 ps.

Based on the above analysis, the interlayer twisting enlarges the lattice parameters and the atom population in the cell. Meanwhile, it also strongly influences the lattice vibrations which causes the decrease of phonon relaxation time. All of these indicate the reduction of thermal conductivity with rotation. For the positive correlation between thermal conductivity and twisting angle above 20° degrees, we believe this is due to the combination of the inherent anisotropy of graphene and the twisting. Therefore, the in-plane anisotropy disappears for the quasi-lattice structure with a twisting angle of 30°.

3.3 Length effect and mean free path

The size effect is one of the most important effects for low-dimensional materials.[44,45] The variation of thermal conductivity with the length for different twisting angles, and the phonon

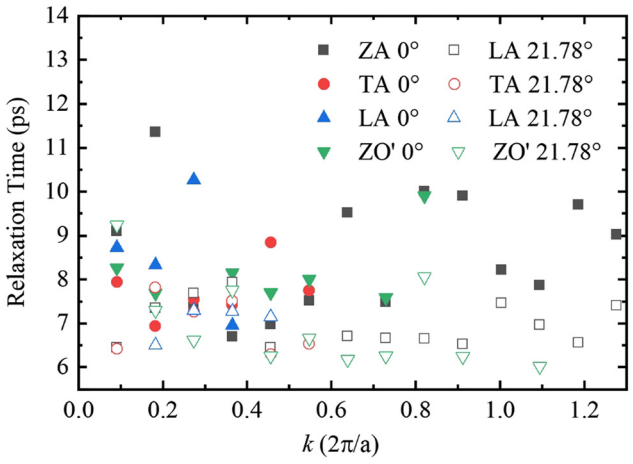

Fig. 8 Relaxation time fitted by Lorentz function of different branches of twisted bilayer graphene while solid points denote bilayer graphene and hollow points represent twisted bilayer graphene with a twisting angle of 21.78°.

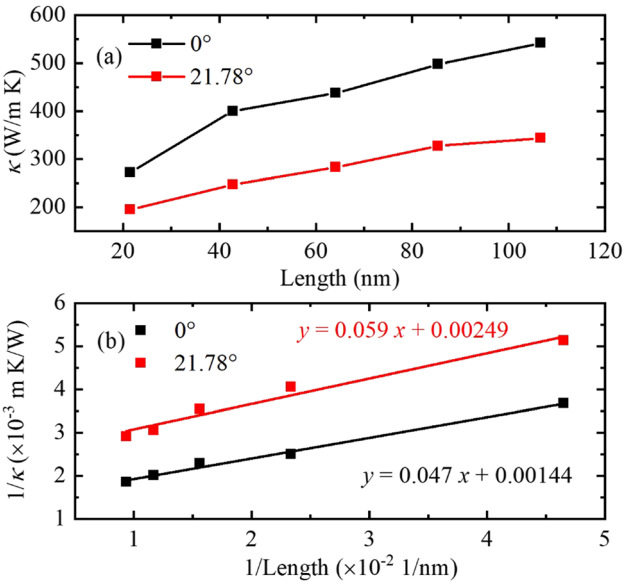

Fig. 9 (a) Variation of thermal conductivity with length and (b) the relationship between the variation of their inverse. The fitting results for bilayer graphene and twisted bilayer graphene are shown in black and red, respectively.

mean free path (MFP) are obtained according to the fitting formula of this relation:[46]

$$\frac{1}{\kappa(L)} = \frac{1}{\kappa_\infty}\left(1 + \frac{\lambda}{L}\right) \quad (9)$$

where L is the length of the structure and λ is the phonon mean free path. The relationship between the length and thermal conductivity is first illustrated in Fig. 9(a). It can be found that whether the bilayer graphene is twisted or not, the thermal conductivity increases with increasing length and gradually converges. In addition, with the increase in length, the thermal conductivity of TBLG is always less than those of bilayer graphene. We also illustrated the relationship diagram of $1/\kappa$ and $1/L$ in Fig. 9(b).

At the same time, the specific equation for the variation of the inverse of the thermal conductivity with the inverse of the length is obtained by linear fitting, $y = 0.047x + 0.00144$ for bilayer graphene, and $y = 0.059x + 0.00249$ for TBLG with a twisting angle of 21.78°, where x and y represent $1/L$ and $1/\kappa$, respectively. Therefore, κ_∞ and λ can be obtained from this fitting equation, 694.44 W m^{-1} K^{-1}, 401.61 W m^{-1} K^{-1} and 32.64 nm, 23.69 nm, respectively. The thermal conductivity and mean free path of bilayer graphene are higher than those of TBLG. These effectively complement and justify the preceding phonon analysis.

4. Conclusions

In summary, a high-fidelity and high-accuracy thermal regulation method is proposed in this work by interlayer twisting in bilayer graphene. The anisotropic thermal conductivity of TBLG with different twisting angles is calculated using the NEMD methods. The thermal conductivity shows a parabolic correlation with the twisting angle. The anisotropic thermal transport is significant in different directions with non-monotonic relationships with the twisting angles, which may be an effective way to regulate the anisotropy of materials. Furthermore, we perform phonon analysis to explain the above phenomenon. The calculated PDOS are distinct along different directions for bilayer graphene but are similar for TBLG with twisting angles of 30°, which support the strong anisotropy of bilayer graphene and convergence at 30°. By calculating the SED, phonon dispersion, and relaxation time are acquired to further reveal the mechanism between the twisting angle and thermal conductivity. The relaxation times of TBLG are lower than those of bilayer graphene, demonstrating the lower thermal conductivity of TBLG. The final mean free path fitted by the length and thermal conductivity relationship confirms the above results.

Conflicts of interest

The authors have no conflict of interest to declare.

Acknowledgements

Y. Y. acknowledges the financial support from the National Natural Science Foundation of China (No. 52076156) and the National Key Research and Development Program of China (No. 2019YFE0119900). The authors appreciate the support from the Supercomputing Center of Wuhan University. J. Z. acknowledges the support from Microsoft Azure.

References

1 A. K. Geim and K. S. Novoselov, *Nat. Mater.*, 2007, **6**, 183–191.
2 A. H. Castro Neto, F. Guinea, N. M. R. Peres, K. S. Novoselov and A. K. Geim, *Rev. Mod. Phys.*, 2009, **81**, 109–162.
3 I. W. Frank, D. M. Tanenbaum, A. M. Van der Zande and P. L. McEuen, *J. Vac. Sci. Technol., B*, 2007, **25**, 2558–2561.
4 A. A. Balandin, *Nat. Mater.*, 2011, **10**, 569–581.
5 K. I. Bolotin, K. J. Sikes, Z. Jiang, M. Klima, G. Fudenberg, J. Hone, P. Kim and H. L. Stormer, *Solid State Commun.*, 2008, **146**, 351–355.
6 A. A. Balandin, S. Ghosh, W. Z. Bao, I. Calizo, D. Teweldebrhan, F. Miao and C. N. Lau, *Nano Lett.*, 2008, **8**, 902–907.
7 T. Ohta, A. Bostwick, T. Seyller, K. Horn and E. Rotenberg, *Science*, 2006, **313**, 951–954.
8 S. Ghosh, W. Z. Bao, D. L. Nika, S. Subrina, E. P. Pokatilov, C. N. Lau and A. A. Balandin, *Nat. Mater.*, 2010, **9**, 555–558.
9 A. Gupta, G. Chen, P. Joshi, S. Tadigadapa and P. C. Eklund, *Nano Lett.*, 2006, **6**, 2667–2673.
10 C. H. Lui, Z. Q. Li, K. F. Mak, E. Cappelluti and T. F. Heinz, *Nat. Phys.*, 2011, **7**, 944–947.
11 Y. B. Zhang, T. T. Tang, C. Girit, Z. Hao, M. C. Martin, A. Zettl, M. F. Crommie, Y. R. Shen and F. Wang, *Nature*, 2009, **459**, 820–823.

12 M. Yankowitz, S. Chen, H. Polshyn, Y. Zhang, K. Watanabe, T. Taniguchi, D. Graf, A. F. Young and C. R. Dean, *Science*, 2019, **363**, 1059–1064.
13 P. Moon and M. Koshino, *Phys. Rev. B: Condens. Matter Mater. Phys.*, 2013, **87**, 205404.
14 W. X. Liu, Y. Q. Wu, Y. Hong, B. Hou, J. C. Zhang and Y. N. Yue, *Phys. Chem. Chem. Phys.*, 2021, **23**, 19166–19172.
15 C. Y. Li, B. Debnath, X. J. Tan, S. S. Su, K. Xu, S. P. Ge, M. R. Neupane and R. K. Lake, *Carbon*, 2018, **138**, 451–457.
16 Y. Cao, V. Fatemi, S. Fang, K. Watanabe, T. Taniguchi, E. Kaxiras and P. Jarillo-Herrero, *Nature*, 2018, **556**, 43–50.
17 G. Tarnopolsky, A. J. Kruchkov and A. Vishwanath, *Phys. Rev. Lett.*, 2019, **122**, 106405.
18 S. Dai, Y. Xiang and D. J. Srolovitz, *Nano Lett.*, 2016, **16**, 5923–5927.
19 F. Symalla, S. Shallcross, I. Beljakov, K. Fink, W. Wenzel and V. Meded, *Phys. Rev. B: Condens. Matter Mater. Phys.*, 2015, **91**, 205412.
20 H. A. Le and V. N. Do, *Phys. Rev. B*, 2018, **97**, 125136.
21 J. Campos-Delgado, L. G. Cancado, C. A. Achete, A. Jorio and J. P. Raskin, *Nano Res.*, 2013, **6**, 269–274.
22 C. Wang, Y. Liu, L. Li and H. Tan, *Nanoscale*, 2014, **6**, 5703–5707.
23 J. Philip, P. Hess, T. Feygelson, J. E. Butler, S. Chattopadhyay, K. H. Chen and L. C. Chen, *J. Appl. Phys.*, 2003, **93**, 2164–2171.
24 Z. Guo, A. Verma, X. F. Wu, F. Y. Sun, A. Hickman, T. Masui, A. Kuramata, M. Higashiwaki, D. Jena and T. F. Luo, *Appl. Phys. Lett.*, 2015, **106**, 111909.
25 J. D. Renteria, S. Ramirez, H. Malekpour, B. Alonso, A. Centeno, A. Zurutuza, A. I. Cocemasov, D. L. Nika and A. A. Balandin, *Adv. Funct. Mater.*, 2015, **25**, 4664–4672.
26 Z. Ye, B. Cao and Z. Guo, *Carbon*, 2014, **66**, 567–575.
27 H. J. Jang, J. D. Wood, C. R. Ryder, M. C. Hersam and D. G. Cahill, *Adv. Mater.*, 2015, **27**, 8017–8022.
28 A. I. Cocemasov, D. L. Nika and A. A. Balandin, *Phys. Rev. B: Condens. Matter Mater. Phys.*, 2013, **88**, 035428.
29 N. N. T. Nam and M. Koshino, *Phys. Rev. B*, 2020, **101**, 099901.
30 S. Plimpion, *J. Comput. Phys.*, 1995, **117**, 1–19.
31 L. Lindsay and D. A. Broido, *Phys. Rev. B: Condens. Matter Mater. Phys.*, 2010, **81**, 205441.
32 A. K. Rappe, C. J. Casewit, K. S. Colwell, W. A. Goddard and W. M. Skiff, *J. Am. Chem. Soc.*, 1992, **114**, 10024–10035.
33 X. Y. Wang, Y. Hong, D. W. Ma and J. C. Zhang, *J. Mater. Chem. C*, 2017, **5**, 5119–5127.
34 Z. X. Guo, D. Zhang and X. G. Gong, *Appl. Phys. Lett.*, 2009, **95**, 163103.
35 W. R. Zhong, M. P. Zhang, B. Q. Ai and D. Q. Zheng, *Appl. Phys. Lett.*, 2011, **98**, 113107.
36 L. Lindsay, D. A. Broido and N. Mingo, *Phys. Rev. B: Condens. Matter Mater. Phys.*, 2011, **83**, 235428.
37 Z. Aksamija and I. Knezevic, *Appl. Phys. Lett.*, 2011, **98**, 141919.
38 J. A. Thomas, J. E. Turney, R. M. Iutzi, C. H. Amon and A. J. H. McGaughey, *Phys. Rev. B: Condens. Matter Mater. Phys.*, 2010, **81**, 081411.
39 J. M. B. L. dos Santos, N. M. R. Peres and A. H. Castro Neto, *Phys. Rev. B: Condens. Matter Mater. Phys.*, 2012, **86**, 155449.
40 J.-W. Jiang, B.-S. Wang and T. Rabczuk, *Appl. Phys. Lett.*, 2012, **101**, 023113.
41 P. Anees, M. C. Valsakumar and B. K. Panigrahi, *2D Mater.*, 2015, **2**, 035014.
42 K. Sato, J. S. Park, R. Saito, C. X. Cong, T. Yu, C. H. Lui, T. F. Heinz, G. Dresselhaus and M. S. Dresselhaus, *Phys. Rev. B: Condens. Matter Mater. Phys.*, 2011, **84**, 035419.
43 J. A. Yan, W. Y. Ruan and M. Y. Chou, *Phys. Rev. B: Condens. Matter Mater. Phys.*, 2008, **77**, 125401.
44 D. P. Sellan, E. S. Landry, J. E. Turney, A. J. H. McGaughey and C. H. Amon, *Phys. Rev. B: Condens. Matter Mater. Phys.*, 2010, **81**, 214305.
45 H. Zaoui, P. L. Palla, F. Cleri and E. Lampin, *Phys. Rev. B*, 2016, **94**, 054304.
46 P. K. Schelling, S. R. Phillpot and P. Keblinski, *Phys. Rev. B: Condens. Matter Mater. Phys.*, 2002, **65**, 144306.

